Accepted Manuscript

Formation and properties of a self-assembled Cu-Fe-Ni-Cr-Si immiscible composite by laser induction hybrid cladding

Xiaoqin Dai, Min Xie, Shengfeng Zhou, Chunxia Wang, Jiaoxi Yang, Zhengyang Li

PII: S0925-8388(18)30405-5

DOI: 10.1016/j.jallcom.2018.01.387

Reference: JALCOM 44851

To appear in: *Journal of Alloys and Compounds*

Received Date: 10 October 2017

Revised Date: 25 January 2018

Accepted Date: 29 January 2018

Please cite this article as: X. Dai, M. Xie, S. Zhou, C. Wang, J. Yang, Z. Li, Formation and properties of a self-assembled Cu-Fe-Ni-Cr-Si immiscible composite by laser induction hybrid cladding, *Journal of Alloys and Compounds* (2018), doi: 10.1016/j.jallcom.2018.01.387.

Graphical abstract

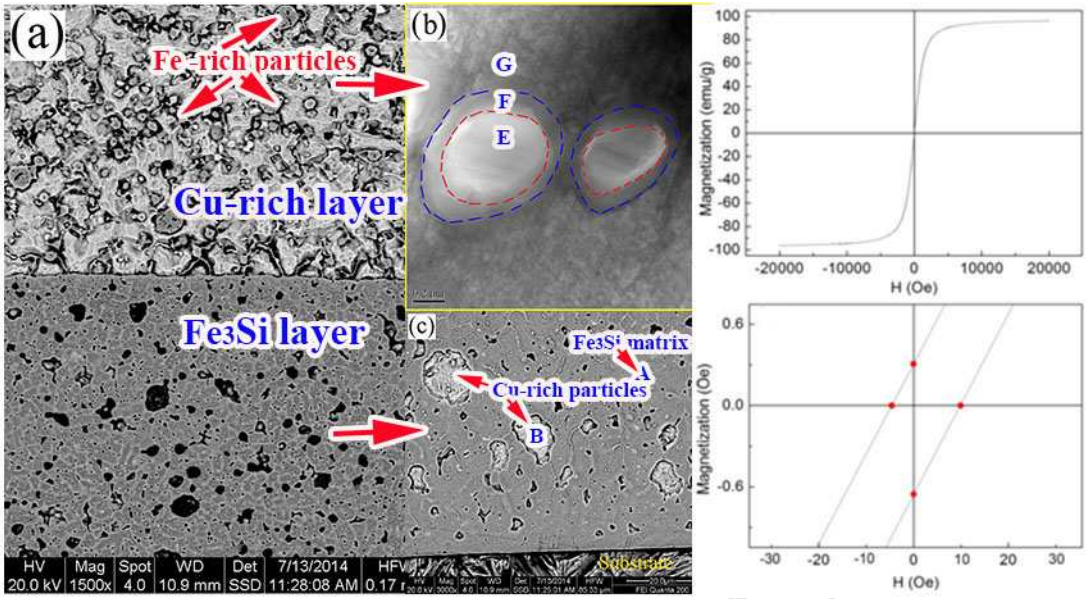

Formation and properties of a self-assembled Cu-Fe-Ni-Cr-Si immiscible composite by laser induction hybrid cladding

Xiaoqin Dai [a*], Min Xie [a], Shengfeng Zhou [a*], Chunxia Wang [b], Jiaoxi Yang [c*], Zhengyang Li [d]

[a] Laser Technology Institute, Tianjin Polytechnic University, Tianjin, 300387, P. R. China

[b] School of Materials science and Engineering, Nanchang Hangkong University, Nanchang, Jiangxi 330063, P. R. China

[c] Institute of Laser Engineering, Beijing University of Technology, Beijing, 100124, P. R. China

[d] Institute of Mechanics, Chinese Academy of Sciences, Beijing 10090, P. R. China

Abstract: A self-assembled Cu-Fe-Ni-Cr-Si immiscible composite with a bilayer structure was produced by laser induction hybrid cladding (LIHC) as a result of liquid phase separation (LPS). The microstructure exhibited by large amounts of ferromagnetic (FM) Fe_3Si particles dispersed within the ε-Cu matrix in the upper layer, and many ε-Cu particles embedded within the FM Fe_3Si matrix in the lower layer. The microhardness values of the Fe_3Si matrix lower layer ($758HV_{0.2}$) and ε-Cu matrix upper layer ($248HV_{0.2}$) were ~7.3 and ~2.4 times higher than that of pure copper by LIHC, respectively, indicating that the immiscible composite exhibited strongly inhomogeneous characteristics consistent with a "bilayer structure". Moreover, the immiscible composite showed a high saturation magnetization of 96.2 emu/g and a low coercivity of 7.24 Oe due to the formation of FM Fe_3Si with micro- and nanoscaled structures.

Keywords: Liquid phase separation (LPS); Magnetization; Microstructure; Bilayer; Immiscible composite

1. Introduction

* Corresponding author.
E-mail address: daixq0827@163.com (X. Dai), zhousf1228@163.com, yangjiaoxi@bjut.edu.cn

When supercooling of Cu-Fe immiscible alloys beyond a certain temperature below the metastable liquid miscible gap (T_{sep}), they can separate into two melts: a Fe-rich melt (L1) and a Cu-rich melt (L2). Subsequently, each melt not only experiences its own supercooling, but also follows a solidification path that is considerably different from that expected for the bulk composition [1, 2]. In particular, when the spherical particles are dispersed in a metallic matrix, the immiscible alloys can exhibit many unique properties and therefore are very promising as self-assembled composites for various industrial applications, such as electronic packaging solder, magnetoresistive materials, advanced bearings in the automotive industry, and metallic phase change materials (PCM) in latent heat storage systems [3-6].

However, there is a density difference between the L1 and L2 melts; therefore, a large segregation takes place prior to solidification, which limits the potential applications of the Cu-Fe immiscible alloys [7]. Therefore, numerous investigations have been performed to examine the factors that affect the solidification process, such as the chemical composition [8], the degree of supercooling [5], the cooling rate [5], the velocities of the Marangoni and Stokes motions [9], and the present alloying elements [10]. The mechanism of liquid phase separation (LPS) generally is related to the interfacial tension, which can induce collisions and coagulation. Even under the microgravity conditions, the Marangoni motion can still result in the colliding and coarsening of the minority phase droplets (MPDs), implying that the rapid growth and coalescence of MPDs are essentially unavoidable [11].

Compared to conventional solidification techniques (e.g., casting), the rapid solidification technique has great potential in the manufacturing of immiscible alloys with a desired microstructure due to its high cooling rate and dynamic supercooling behaviour, which has received considerable attention. Specifically, when Wang et al. [12] reported that an egg-type or core-shell microstructure can

be obtained in the immiscible Cu-Fe-Si alloy powder by gas atomization, an efficient solution was opened for broadening the application of immiscible alloys. For instance, Koziel et al. [13] produced crystalline Cu-rich spherical precipitates dispersed in an amorphous Fe-rich matrix by melt spinning at a cooling rate of ~10^5 K/s. Nagase et al. [14] found that the spherical face-centered-cubic (fcc)-Cu crystalline precipitates formed within an Fe-rich amorphous matrix when the Fe-Cu-Zr-B immiscible alloys were produced by melt-spinning. Ziewiec et al. [15] also found similar microstructural characteristics and phase transformation behaviour in $Fe_{60}Cu_{20}P_{10}Si_5B_5$ immiscible alloy that was fabricated using melt-spinning. Zhang et al. [16] also reported a core-shell (CS) structured Ti alloy with isolated soft coarse-grained Ti cores and hard Ti-O solid solution shells.

Recently, laser induction hybrid cladding has been used to produce Cu-Fe immiscible composites [17-19]. It was found that the microstructure and properties not only depend on the inoculant addition of CNTs [17], and the alloying element addition of Al [10], but also depend on the substrate type and laser scanning speed [18, 19]. Although most researchers [1-14, 20] have focused on the solidification dynamics and the mechanisms of LPS in immiscible Cu-Fe bulk alloys, no studies reported the soft magnetic properties of an immiscible Cu-Fe composite with a bilayer structure. In the present paper, a high laser scanning speed was used to produce a Si-rich Cu-Fe-Ni-Cr-Si immiscible composite. The emphasis of this study was to investigate the phase separation characteristics, microhardness and soft magnetic properties of a self-assembled Cu-Fe-Ni-Cr-Si immiscible composite.

2. Experimental procedures

Low carbon steel with dimensions of 120 mm × 60 mm × 5 mm was used as the substrate. The Cu-Fe-Ni-Cr-Si alloy powder was used as the cladding material which was composed of 58.5 wt.% pure copper powder, 31.5 wt.% Fe-12Ni-5Cr-0.6Si-0.2C powder, and 10 wt.% pure Si powder. The

average sizes of the Cu, Fe alloy and Si powders were 40 μm, 45 μm and 35 μm, respectively. The processing apparatus for laser induction hybrid cladding has been previously described in detail [21]. The processing parameters were as follows: 5 kW laser power, 3500 mm/min laser scanning speed, 4 mm spot diameter, 50% overlapping rate, 103.6 g/min powder feeding rate, 53° angle between the powder nozzle and the substrate [22], and 1173 K preheated temperature of the substrate. A shield of Ar gas was used to blow the cladding material into the molten pool and shield the molten pool. The dimension o α f the produced cladding layer was 80 mm × 20 mm × 1.0 mm.

After LIHC, the metallurgical sample was prepared and etched by a solution of 5 g $FeCl_3$, 15 ml HCl and 100 ml H_2O. The microstructure was observed by a Quanta 200 environmental scanning electron microscopy (ESEM) with energy-dispersive spectroscopy (EDS). The phase constituents were investigated by X-ray diffraction (XRD, Cu Kα radiation at 40 kV/40 mA, scan rate: 0.02°/s). To investigate the fine scale structures, the immiscible composite was peeled off the substrate and studied by transmission electron microscopy (TEM). TEM images were taken using a JEOL-2100F TEM operated at 200 kV. The chemical compositions were studied by X-ray energy-dispersive spectrometry (EDS) attached to the TEM. The microhardness of the immiscible composite was measured in a digital Vickers hardness tester with a load of 1.96 N and a dwell time of 30 s. The magnetic properties were measured repeatedly by an MPMS XL vibrating sample magnetometer at room temperature with a maximum applied field of 20,000 Oe.

3. Results and discussion

Fig. 1 shows the X-ray diffraction pattern of the immiscible composite. The phase constituents are composed of ε-Cu, Fe_3Si and (Fe, Ni). The ε-Cu and Fe_3Si constituents exhibit a face-centered cubic (fcc) structures, while the (Fe, Ni) has a hexagonal structure. According to references [23-25],

additional analyses can be conducted on the XRD data in Fig. 1. For instance, the crystallite sizes of ε-Cu (lattice parameter: 0.3615 nm), Fe_3Si (lattice parameter: 0.5655 nm) and (Fe, Ni) (lattice parameter: a=0.2485 nm, c=0.403 nm) phases are ~30.332 nm, ~21.426 nm and ~15.265 nm, respectively. The volume fractions of ε-Cu, Fe_3Si and (Fe, Ni) phases are ~79.2%, ~17.3% and ~3.5%, respectively.

Fig. 2 shows the SEM images of the immiscible composite. It is apparent that the bilayer structure is composed of Cu-rich particles embedded within the Fe-rich matrix in the lower layer and Fe-rich particles embedded within the Cu-rich matrix in the upper layer (Fig. 2a). According to the XRD (Fig. 1) and EDS (Table 1) results, the Cu-rich particles and Cu-rich matrix have a similar chemical composition so that they can be identified as Cu-rich ε-Cu that contains large amounts of Ni, Si and Fe. Similarly, the Fe-rich particles and Fe-rich matrix can be identified as the intermetallic compound (IMC) Fe_3Si containing large amounts of Cu. Moreover, the Fe_3Si matrix (marked A in Fig. 2b) presents the growth of columnar dendrites at the composite-substrate interface and many spherical ε-Cu particles (marked B in Fig. 2b) are dispersed in the interdendrites. The elongated Fe_3Si dendrites with a length of ~10 μm and a width of ~5 μm are formed at the top of the Fe-rich layer, and large amounts of nanoscaled Cu-rich grains are precipitated inside these Fe_3Si dendrites, as shown in Fig. 2c and d. However, large amounts of ~15-μm-diameter spherical Fe_3Si particles (marked D in Fig. 2e) are embedded homogeneously into the ε-Cu matrix (marked C in Fig. 2e). Many white nanoscaled Cu-rich grains are also precipitated inside the larger Fe_3Si particles due to secondary liquid phase separation (SLPS). Those larger Fe_3Si particles are formed at the expense of small Fe-rich particles via collision and coarsening behaviours (Fig. 2f)

To investigate the fine structure of the immiscible composite, TEM images of the Fe-rich particles

and Cu-rich matrix in the upper layer were acquired, and the results are shown in Fig. 3. Obviously, the Fe-rich particles present a core-shell structure with a diameter of ~500 nm. According to the EDS analysis results (Table 2), the core structure (marked E in Fig. 3a) is rich in Fe and Ni, and contains large amounts of Cu and Si, whereas the shell structure (marked F in Fig. 3a) is rich in Cu and contains large amounts of Ni. These results indicate that an interface with a thickness of ~50 nm (marked G in Fig. 3a) is formed between the Fe-rich particles and the Cu-rich matrix by a diffusion mechanism [26]. Based on the XRD (Fig. 1) and EDS (Table 2) results, the core-shell particles can be identified as Fe_3Si with a lattice constant of 0.5655 and a $D0_3$-type structure (Fig. 3b) [27]. Furthermore, large amounts of dislocation loops are distributed in the fcc ε-Cu matrix containing ~5 at.% Si. The formation of an fcc-Cu structure was also reported in Fe-Cu-Si-based immiscible alloys by Luo et al. [28] and Nagase et al. [29], because the solubility of Si in fcc-Cu is significantly large reaching 10 at.% in the thermally equilibrated Cu-Si alloys [30].

Fig. 4 shows a TEM image of nanostructured grains precipitated inside the Fe_3Si dendrite in the lower layer. Based on the chemical composition (Table 3), the nanostructured grains (marked I) can be ε-Cu containing a large amount of Fe and small amounts of Ni and Cr. The dendrite (marked H) contains ~16 wt.% Si, large amounts of Fe and Ni, which is confirmed to be Fe-rich Fe_3Si. This result indicates that the nanograins of ε-Cu are precipitated inside the Fe-rich Fe_3Si dendrites due to secondary liquid phase separation (SLPS). Moreover, some nanostructured particles are also observed in the ε-Cu matrix in the upper layer, and a typical TEM image is shown in Fig. 5a. It can be seen that the nanostructured particles also exhibit a core-shell structure. According to the composition mapping results (Fig. 5b~f), the core region contains a large amount of Ni and Fe, but small amounts of Si and Cu. The shell region is rich in Fe, and small amounts of Cu can diffuse into this region. Combined with

the XRD analysis results (Fig. 1), the nanostructured particles can be (Fe, Ni) phase with a Ni-rich core/Fe-rich shell structure.

The previous results [19, 21] have shown that the cooling rate is at a level of 10^4-10^5 K/s during LIHC, which is still a rapid solidification process. This, in turn, can induce a dynamic supercooling at a temperature larger than 150 K, which is much higher than the temperatures from 80-100 K required for Cu-Fe immiscible alloys containing 40-65 wt.% Cu [31]. As a result, the supercooled Cu-Fe-Ni-Cr-Si alloy liquid will be thermodynamically unstable and can enter into the miscible gap rapidly to separate into two melts: an Fe-rich melt (L1) and a Cu-rich melt (L2). Because L1 has relatively better wettability with the Fe-rich substrate than does L2, L1 will sink to the lower part of the molten pool [18]. Generally, the radius of the critical nucleation and the formulation work of the critical crystal nucleus can respectively be described as [2, 5]:

$$r^* = \frac{2\gamma \cdot T_m}{L_m \cdot \Delta T} \tag{1}$$

$$\Delta G^* = \frac{16\pi\gamma^3 \cdot T_m^3}{3L_m^2 \cdot \Delta T^2} \tag{2}$$

where r^* is the radius of the critical crystal nucleus, ΔG^* is the formulation work of the critical crystal nucleus, γ is surface energy per unit area of embryos, T_m is the melting temperature of the melt, ΔT is the supercooling of the melt, and L_m is the latent heat of the liquid-solid phase transformation. According to the Cu-Fe binary phase diagram [32], the L1 melt always demonstrates a more developed supercooling behaviour than does the L2 melt. According to the Eqs. (1) and (2), L1 has a smaller radius (r^*) and formulation work (ΔG^*) of the critical nucleation compared to that of L2, implying that L1 will solidify before L2. Therefore, L1 starts to solidify at the bottom of the molten pool. When L1 finishes its solidification, L2 grows on the surface of the solidified Fe-rich layer to form the Cu-rich upper layer, leading to a bilayer structure (Fig. 2a).

In fact, the L1 and L2 will go through their own solidification paths which depend on the chemical composition, the supercooling occurring prior to solid nucleation, the cooling rate and fluid flow after liquid phase separation (LPS) [2]. To minimize the surface energy, the L1 droplets begin to form in the upper L2 region of the molten pool. Similarly, the L2 droplets form in the lower L1 region of the molten pool. These droplets can move, collide and impinge with each other within the liquid matrix due to Marangoni motion and Stokes motion. Generally, the velocity of liquid droplets driven by Marangoni motion is ~10^4 times faster than that driven by Stokes motion [12], suggesting that the Stokes effect can be ignored. For a simple qualitative analysis, the velocity of the liquid droplets induced by Marangoni motion is estimated as follows [12]:

$$v_m = \frac{2r_d}{3(3\eta_d + 2\eta_d)} \cdot \frac{\partial \sigma}{\partial T} \cdot G \tag{3}$$

where r_d is the radius of the liquid droplet, G is the temperature gradient, η_d and η_m are the viscosities of the liquid droplet and the liquid matrix, respectively, and the $\frac{\partial \sigma}{\partial T}$ is the interfacial energy. Therefore, the spherical droplets can grow into the larger droplets by a diffusion-coupling mechanism or a gradient induced coupling mechanism [33]. The larger droplets will be susceptible to move towards the top of the molten pool due to a relatively larger velocity induced by Marangoni motion according to Eq. (3). As a result, some relatively larger Cu-rich particles will form at the top region of the Fe-rich Fe_3Si lower layer and some relatively larger Fe-rich Fe_3Si particles form at the top region of the Cu-rich matrix upper layer after rapid solidification, as shown in Fig. 2b and f.

According to the XRD and TEM analysis results, the intermetallic compound (IMC) Fe_3Si is formed both in the lower layer as the metallic matrix and in the upper layer as spherical particles. The Fe-Si phase diagram shows that the D03 type Fe_3Si phase is stable over a wide composition range (Si content of 11-25 at.%) at 873-973 K [34]. Moreover, the standard Gibbs free energy calculation for a

Fe-rich silicide phase at 973 K indicates that stoichiometric Fe_3Si is the most stable composition and can form preferentially compared to Fe_2Si and FeSi [35]. Generally, the crystal structure of a D03-type large Fe_3Si nanoparticle is derived based on the space group *Fm-3m* and the cubic unit-cell dimension of 0.5655 nm. Thus, spheroidal Fe_3Si nanoparticles in a Cu-rich ε-Cu matrix are significantly different from that of D03-type Fe_3Si randomly oriented nanocrystals in amorphous $Fe_{73.5}Si_{15.5}Cu_1Nb_3B_7$ ribbons [36]. Dahal et al. [37] also found that the similar spherical Fe_3Si nanoparticles can be produced by a high-temperature reduction method. Therefore, L1 as the major melt can form an Fe_3Si matrix in the lower layer (Fig. 2c and d), while L1 as the minor melt can form spherical Fe_3Si particles in the upper layer (Fig. 2e and f). Generally, the solubility of Cu in the Fe_3Si phase is negligible [38]. When the heat removal rate falls behind the rate at which latent heat is released due to L2 solidification, the secondary liquid phase separation (SLPT) of the Fe-rich Fe_3Si phase is induced during LIHC because the temperature increase from the release of the crystallization latent heat of L2 is sufficient to exceed the T_{sep}. As a result, the nanoscaled Cu-rich grains are precipitated inside the Fe_3Si phase (Figs. 2d, 2f and 4).

Fig. 6 shows the microhardness profile of the immiscible composite. It can be seen that the immiscible composite exhibits a sharp gradient distribution of microhardness, which is in accordance with the bilayer structure. Furthermore, the IMC Fe_3Si matrix in the lower layer and the ε-Cu matrix in the upper layer both present homogeneous microhardness characteristics. However, the average microhardness of the former ($758HV_{0.2}$) is three times higher than that of the latter ($248HV_{0.2}$). The formation of hard IMC Fe_3Si can improve the microhardness of the Fe-rich lower layer. Many spherical ε-Cu particles (marked B in Fig. 2b) dispersed in the interdendrites can further strengthen the Fe-rich lower layer, due to dispersion strengthening. Moreover, the microhardness of the Cu-rich upper layer is

approximately 2.4 times higher than that of pure copper by LIHC ($104HV_{0.2}$), mainly because large amounts of hard IMC Fe_3Si particles are dispersed within the Cu-rich upper layer, leading to dispersion strengthening. Additionally, the Cu-rich upper layer contains a supersaturation of Fe and a significant amount of Cr (Table 1), resulting in solid solution strengthening. Especially, the rapid solidification during LIHC can often induce compressive residual stresses. These stresses are increased by the high supersaturation of IMC Fe_3Si particles and crystal distortion, leading to the formation of dislocation tangle (Fig. 3a). These dislocations in turn improve the microhardness of the Cu-rich upper layer. Therefore, the improved microhardness of the Cu-rich upper layer is attributed to the combination mechanisms of dispersion strengthening, solid solution strengthening and dislocation strengthening.

Fig. 7 shows the magnetic hysteresis loop of the immiscible composite at 300 K. The saturated magnetization, M_s, occurs at 96.2 emu/g when the magnetic field is larger than 10,000 Oe. Moreover, the corresponding coercively (H_C) is only 7.24 Oe. In comparison, Wang et al. [39] produced $CoCrCuFeNiTi_x$ high-entropy alloys by arc melting and found that their M_s was lower than 2 emu/g. Zhang et al. [40] investigated the magnetic properties of a 6FeNiCoSiCrAlTi high-entropy alloy coating produced by laser cladding and found that the M_s and H_C were 20.04 emu/g and 53.39 Oe, respectively. Generally, the ferromagnetic (FM) Fe_3Si phase has an fcc D03 structure, which can be considered as a Heusler alloy because it has two distinct crystallographic and magnetic Fe sites (Fig. 3c). Moreover, certain Heusler alloys are predicted to be 100% spin polarized at the Fermi level (i.e., they exhibit half-metallic behaviour) [35]. Therefore, the phase separation, which results in FM Fe_3Si particles embedded in the Cu-rich matrix at the upper layer and Cu-rich particles dispersed in the FM Fe_3Si matrix in the lower layer, and the formation of an FM Fe_3Si phase with a proper micro- or nanoscaled structure can help to achieve higher saturated magnetization (M_s) and lower coercivity (H_c),

as shown in the inset of Fig. 7, compared to the soft magnetic properties of high-entropy alloys with a soft ferrite phase.

4. Conclusions

A self-assembled Cu-Fe-Ni-Cr-Si immiscible composite is produced by laser induction hybrid cladding as a result of liquid phase separation. The bilayer structure is composed of many Cu-rich ε-Cu particles dispersed within the Fe-rich Fe_3Si matrix in the lower layer, and large amounts of Fe_3Si particles embedded within the Cu-rich ε-Cu matrix in the upper layer. Some nanoscaled (Fe, Ni) phases with a Ni-rich core/Fe-rich shell structure also precipitate in the Cu-rich upper layer. The microhardness of the Fe_3Si lower layer ($758HV_{0.2}$) is three times higher than that of the ε-Cu matrix upper layer ($248HV_{0.2}$), indicating a sharply changing distribution consistent with a bilayer structure. The improved microhardness of the immiscible composite is attributed to the combination of solid solution strengthening, dispersion strengthening and dislocation strengthening. Furthermore, the immiscible composite exhibits a high saturation magnetization (96.2 emu/g) and a low coercivity (7.24 Oe) due to the formation of ferromagnetic Fe_3Si with a micro- and nanoscaled structure.

Acknowledgements

This work was financially supported by the National Natural Science Foundation of China (Grant No. 51471084), the Outstanding Youth Foundation of Jiangxi Province (20162BCB23039) and the Natural Science Foundation of Tianjin (17JCZDJC40500).

References

[1] A. Munitz, A. Venkert, P. Landau, M. J. Kaufman, R. Abbaschian, Microstructure and phase selection in supercooled cooper alloys exhibiting metastable liquid miscibility gaps, J. Mater. Sci. 47 (2012) 7955-7970.

[2] J. Zhang, X. Cui, Y. Yang, Y. Wang, Solidification of the Cu-35 wt pct Fe alloys with liquid separation, Metall. Mater. Trans. A 44 (2013) 5544-5548.

[3] R. P. Shi, C. P. Wang, D. Wheeler, X. J. Liu, Y. Wang, Formation mechanisms of self-organized core/shell and core/shell/corona microstructures in liquid droplets of immisicible alloys, Acta Mater. 61 (2013) 1229-1243.

[4] B. Ma, J. Li, Z. Peng, G. Zhang, Structural morphologies of Cu-Sn-Bi immiscible alloys with varied compositions, J. Alloys Compd, 535 (2012) 95-101.

[5] A. Munitz, A. M. Bamberger, S. Wannaparhun, R. Abbaschian, Effects of supercooling and cooling rate on the microstructure of Cu-Co-Fe alloys, J. Mater. Sci. 41 (2006) 2749-2759.

[6] B. Ma, J. Li, Z. Xu, Z. Peng, Fe-shell/Cu-core encapsulated metallic phase change materials prepared by aerodynamic levitation method, Appl. Energ. 132 (2014) 568-574.

[7] I. Ohnuma, T. Saegusa, Y. Takaku, C. P. Wang, X. J. Liu, R. Kainuma, K. Ishida, Microstructural evolution of alloy powder for electronic materials with liquid miscibility gap, J. Electron. Mater. 38 (2009) 2-9.

[8] M. Hino, T. Nagasaka, T. Washizu, Phase diagram of Fe-Cu-Si ternary system above 1523 K, J. Phase. Equil. 20 (1999) 179-186.

[9] C. P. Wang, X. J. Lu, R. P. Shi, C. Shen, Y. Wang, I. Ohnuma, R. Kainua, K. Ishida, Design and formation mechanism of self-organize core/shell structure composite powder in immiscible liquid system, Appl. Phys. Lett. 91 (2007) 141904.

[10] S. Zhou, X. Dai, Z. Xiong, C. Wu, T. Zhang, Z. Zhang, Influence of Al addition on microstructure and properties of Cu-Fe-based coatings by laser induction hybrid rapid cladding, J. Mater. Res. 29 (2014) 865-873.

[11] Y. Ruan, Q. Q. Wang, Shou-Yi Chang, B. Wei, Structural evolution and micromechanical properties of ternary Al-Ag-Ge alloy solidified under microgravity condition. Acta Mater. 141 (2017) 456-465.

[12] C. P. Wang, X. J. Liu, I. Ohnuma, R. Kainuma, K. Ishida, Formation of immiscible alloy powders with egg-type microstructure, Science 297 (2002) 990-993.

[13] T. Koziel, Z. Kedzierski, A. Z. Lipiec, K. Ziewiec, The microstructure of liquid immiscible Fe-Cu-based in situ formed amorphous/crystalline composite, Scripta Mater. 54 (2006) 1991-1995.

[14] T. Nagase, M. Suzuki, T. Tanaka, Formation of nanoglobules with core-shell structure by liquid phase separation in Fe-Cu-Zr-B immiscible alloy, J. Alloys Compd. 619 (2015) 332-337.

[15] K. Ziewiec, M. Wojciechowska, G. Garzel, T. Czeppe, A. Błachowski, K. Ruebenbauer, Microstructure and phase transformations in a liquid immiscible $Fe_{60}Cu_{20}P_{10}Si_5B_5$ alloy, Intermetallics 69 (2016) 47-53.

[16] Y. S. Zhang, X. Wang, W. Zhang, W. T. Zhang, W. T. Huo, J. J. Hu, L. C. Zhang, Elevated tensile properties of Ti-O alloy with a novel core-shell structure, Mater. Sci. Eng. A 696 (2017) 360-365.

[17] S. Zhou, C. Wu, T. Zhang, Z. Zhang, Carbon nanotube- and Fe_p-reinforced copper-matrix composites by laser induction hybrid rapid cladding, Scripta Mater. 76 (2014) 25-28.

[18] X. Dai, S. Zhou, M. Wang, J. Lei, M. Xie, H. Chen, C. Wang, T. Wang, Effect of substrate types on the microstructure and properties of Cu65Fe35 composite coatings by laser induction hybrid cladding, J. Alloys Compd. 722 (2017) 173-182.

[19] X. Dai, S. Zhou, M. Wang, J. Lei, C. Wang, T. Wang, Microstructure evolution of phase separated Fe-Cu-Cr-C coatings by laser induction hybrid cladding, Surf. Coat. Technol. 324 (2017) 518-525.

[20] J. He, J. Zhao, L. Ratke, Solidification microstructure and dynamics of metastable phase

transformation in undercooled liquid Cu-Fe alloy, Acta Mater. 54 (2006) 1749-1757.

[21] S. Zhou, Y. Huang, X. Zeng, Q. Hu, Microstructure characteristics of Ni-based WC composite coatings by laser induction hybrid rapid cladding, Mater. Sci. Eng. A 480 (2008) 564-572.

[22] S. Zhou, X. Dai, H. Zheng, Analytical modeling and experimental investigation of laser induction hybrid rapid cladding for Ni-based WC composite coatings, Opt. Laser Technol. 43 (2011) 613-621.

[23] S. Ehtemam-Haghighi, Y. Liu, G. Cao, L. C. Zhang, Influence of Nb on the β→α" martensitic phase transformation and properties of the newly designed Ti-Fe-Nb alloys, Mater. Sci. Eng. C 60 (2016) 503-510.

[24] S. Ehtemam-Haghighi, Y. Liu, G. Cao, L. C. Zhang, Phase transition, microstructure evolution and mechanical properties of Ti-Nb-Fe alloys induced by Fe addition, Mater. Des. 97 (2016) 279-286.

[25] L. C. Zhang, Z. Q. Shen, J. Xu, Glass formation in a (Ti,Zr,Hf)-(Cu,Ni,Ag)-Al high-order alloy system by mechanical alloying, J. Mater. Res. 18 (2003) 2141-2149.

[26] P. Yu, L. C. Zhang, W. Y. Zhang, J. Das, K. B. Kim, J. Eckert, Interfacial reaction during the fabrication of $Ni_{60}Nb_{40}$ metallic glass particles-reinforced Al based MMCs, Mater. Sci. Eng. A 444 (2007) 206-213.

[27] S. Noor, I. Barsukov, M. S. Özkan, L. Elbers, N. Melnichak, J. Lindner, M. Farle, U. Kohler, Surface morphology and atomic structure of thin layers of Fe_3Si on GaAs (001) and their magnetic properties, J. Appl. Phys. 113 (2013) 103908.

[28] S. B. Luo, W. L. Wang, Z. C. Xia, Y. H. Wu, B. Wei, Solute redistribution during phase separation of ternary Fe-Cu-Si alloy, Appl. Phys. A 119 (2015) 1003-1011.

[29] T. Nagase, M. Suzuki, T. Tanaka, Formation of amorphous phase with crystalline globules in Fe-Cu-Si-B and Fe-Cu-Zr-B immiscible alloys, Intermetallics 61 (2015) 56-65.

[30] B. Hassstedt, J. Gröbner, M. Hampl, R. Schmid-Fetzer, Calorimetric measurements and assessment of the binary Cu-Si and ternary Al-Cu-Si phase diagrams, Calphad, 53 (2016) 25-38.

[31] A. Munitz, Liquid separation effects in Fe-Cu alloys solidified under different cooling rates, Metall. Mater. Trans. B 18 (1987) 565-575.

[32] Y. Y. Chuang, R. Schmid, Y. A. Chang, Thermodynamic analysis of the iron-copper system I: The stable and metastable phase equilibria, Metall. Trans. A, 15 (1984) 1921-1930.

[33] H. Tanaka, A new coarsening mechanism of droplet spinodal decomposition, J. Chem. Phys. 103 (1995) 2361-2364.

[34] J. Herfort, H. Schönherr, K. H. Ploog, Epitaxial growth of Fe_3Si/GaAs (001) hybrid structures, Appl. Phys. Lett. 83 (2003) 3912-3914.

[35] Y. Zhang, D. G. Ivey, Fe_3Si formation in Fe-Si diffusion couples, J. Mater. Sci. 33 (1998) 3131-3135.

[36] K. G. Pradeep, G. Herzer, P. Choi, D. Raabe, Atom probe tomography study of ultrahigh nanocrystallization rates in FeSiNbBCu soft magnetic amorphous alloys on rapid annealing, Acta Mater. 68 (2014) 295-309.

[37] N. Dahal, V. Chikan, Phase-controlled synthesis of iron silicide (Fe_3Si and $FeSi_2$) nanoparticles in solution, Chem. Mater. 22 (2010) 2892-2897.

[38] N. Mattern, A. Danzig, M. Müller, Effect of Cu and Nb on crystallization and magnetic properties of amorphous $Fe_{77.5}Si_{15.5}B_7$ alloys, Mater. Sci. Eng. A 194 (1995) 77-85.

[39] X. F. Wang, Y. Zhang, Y. Qiao, G. L. Chen, Novel microstructure and properties of multicomponent $CoCrCuFeNiTi_x$ alloys, Intermetallics 15 (2007) 357-362.

[40] H. Zhang, Y. Pan, Y. He, H. Jiao, Microstructure and properties of 6FeNiCoSiCrAlTi high-entropy

alloy coating prepared by laser cladding, Appl. Surf. Sci. 257 (2011) 2259-2263.

Tables

Table 1 Chemical composition of microstructure in the Cu-Fe-Ni-Cr-Si immiscible composite (Fig. 2).

Zone	Chemical composition (at.%)				
	Si	Fe	Cr	Ni	Cu
A	18.55	64.29	4.57	6.35	6.24
B	3.91	10.29	2.32	4.76	78.82
C	4.66	8.98	3.45	2.05	80.86
D	20.44	58.99	5.60	5.62	9.35

Table 2 Chemical composition of core-shell particles and matrix in the Cu-rich layer (Fig. 3).

Zone	Chemical composition (wt.%)				
	Si	Fe	Cr	Ni	Cu
E	12.39	44.55	4.30	26.22	12.54
F	4.55	2.64	0.32	10.54	81.94
G	2.08	2.31	0.37	2.05	93.20

Table 3 Chemical composition of nanostructured grain precipitated inside the dendrites in the lower layer (Fig. 4).

Zone	Chemical composition (wt.%)				
	Si	Fe	Cr	Ni	Cu
H	15.97	48.16	5.93	21.38	8.56
I	3.87	12.71	1.56	5.64	76.23

Figures

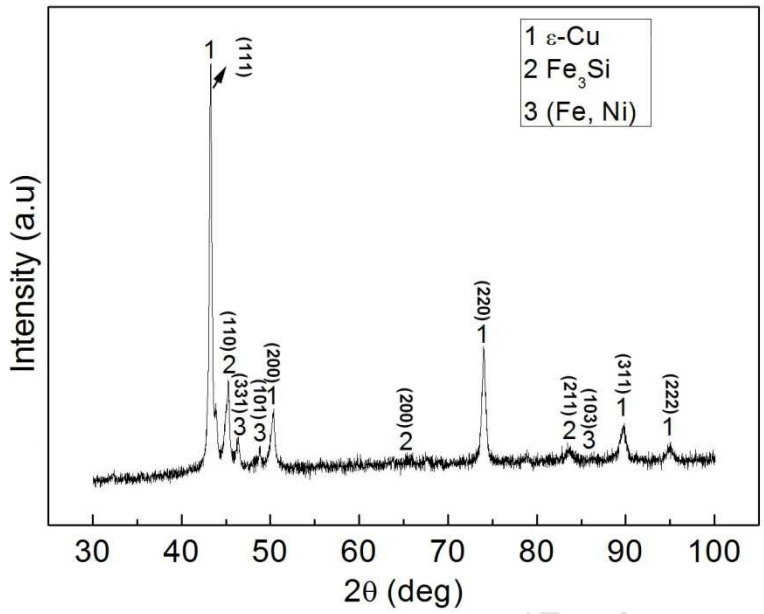

Fig. 1 X-ray diffraction (XRD) pattern of Cu-Fe-Ni-Cr-Si immiscible composite.

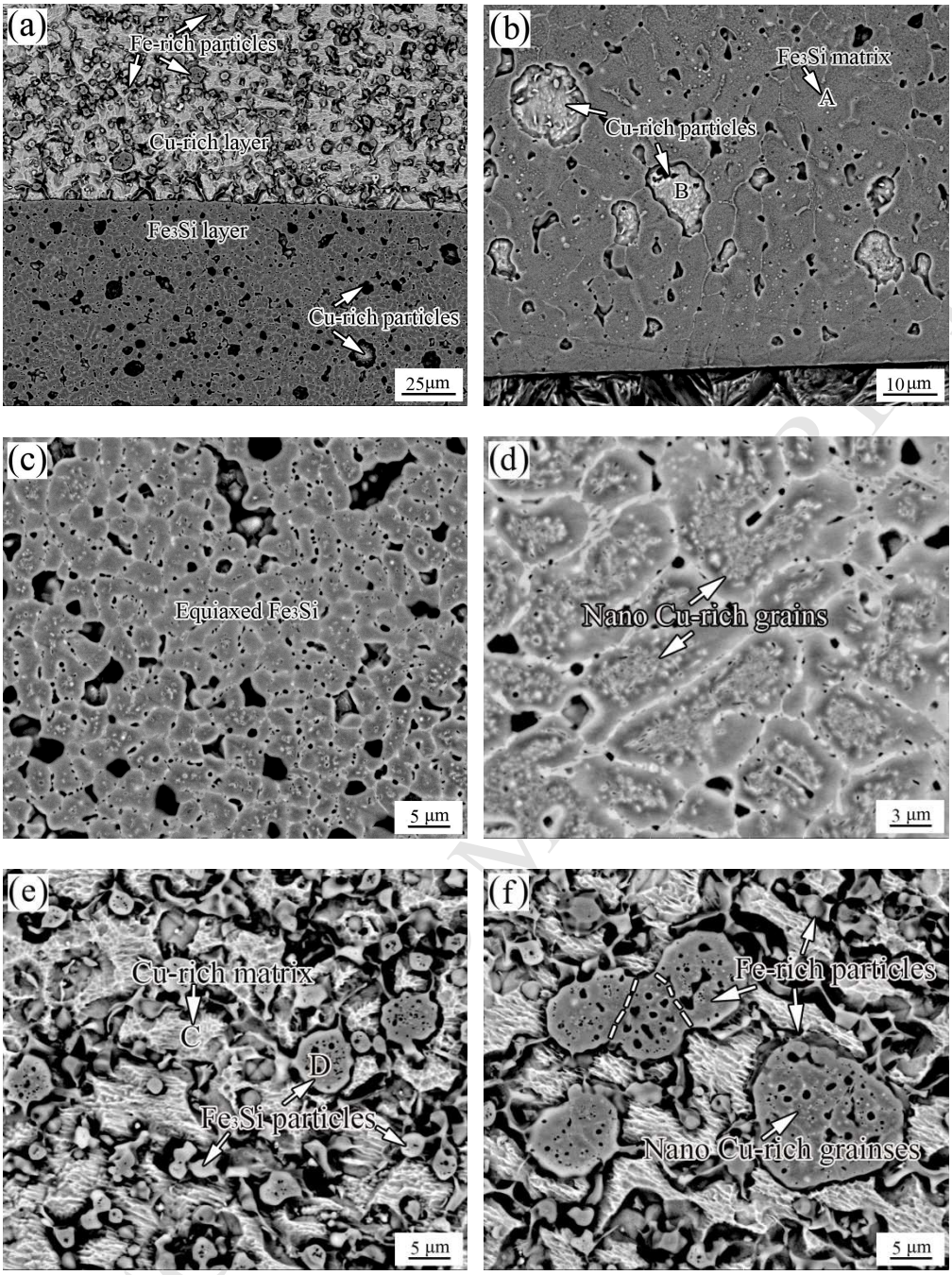

Fig. 2 (a) Interfacial morphology of the Cu-rich layer and Fe_3Si layer, (b) microstructure of the Fe_3Si layer at the composite-substrate interface, (c) microstructure in the upper of Fe_3Si layer, (d) nano-scaled Cu-rich grains precipitated in the Fe_3Si layer, (e) microstructure of the Cu-rich layer, (f) microstructure of the Fe_3Si particles with nano Cu-rich grains in the Cu-rich layer.

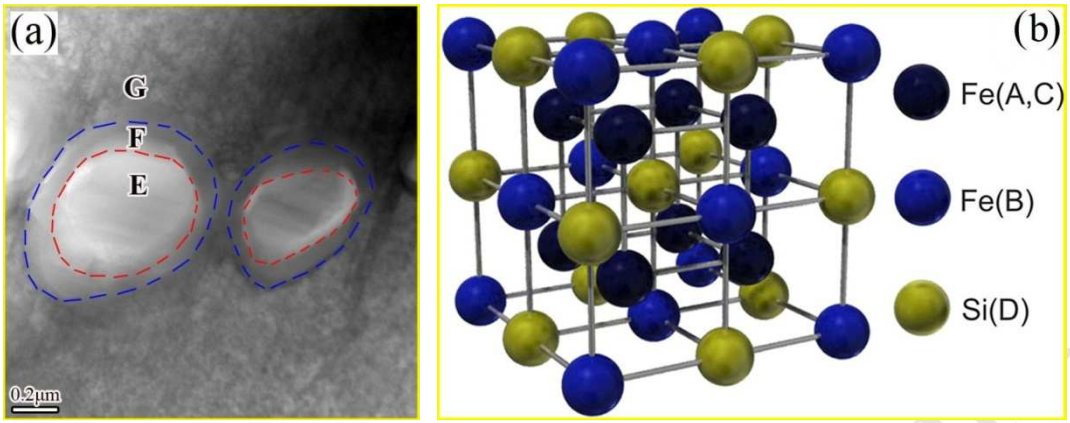

Fig. 3 (a) TEM image of core-shell Fe-rich particles in the Cu-rich matrix, (b) structure of the D03 unit cell of Fe_3Si (Two of the fcc sublattices are occupied by Fe_A atoms, and the other sublattices are occupied by Fe_B and Si, respectively. The A and C sites are equivalent and are occupied by Fe. The B sites are also occupied by Fe, whereas the D sites are occupied by Si [27].

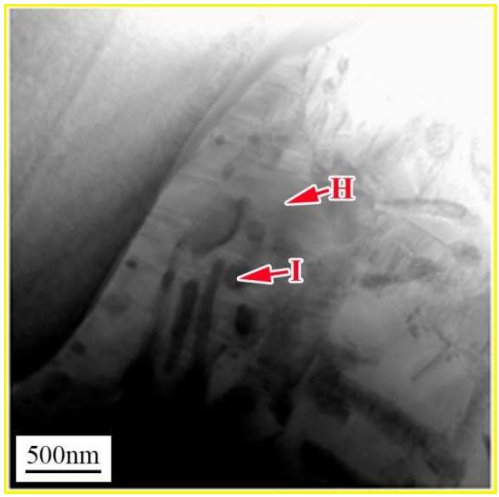

Fig. 4 TEM image of nano-scaled Cu-rich grains precipitated inside the Fe_3Si dendrite in the lower layer.

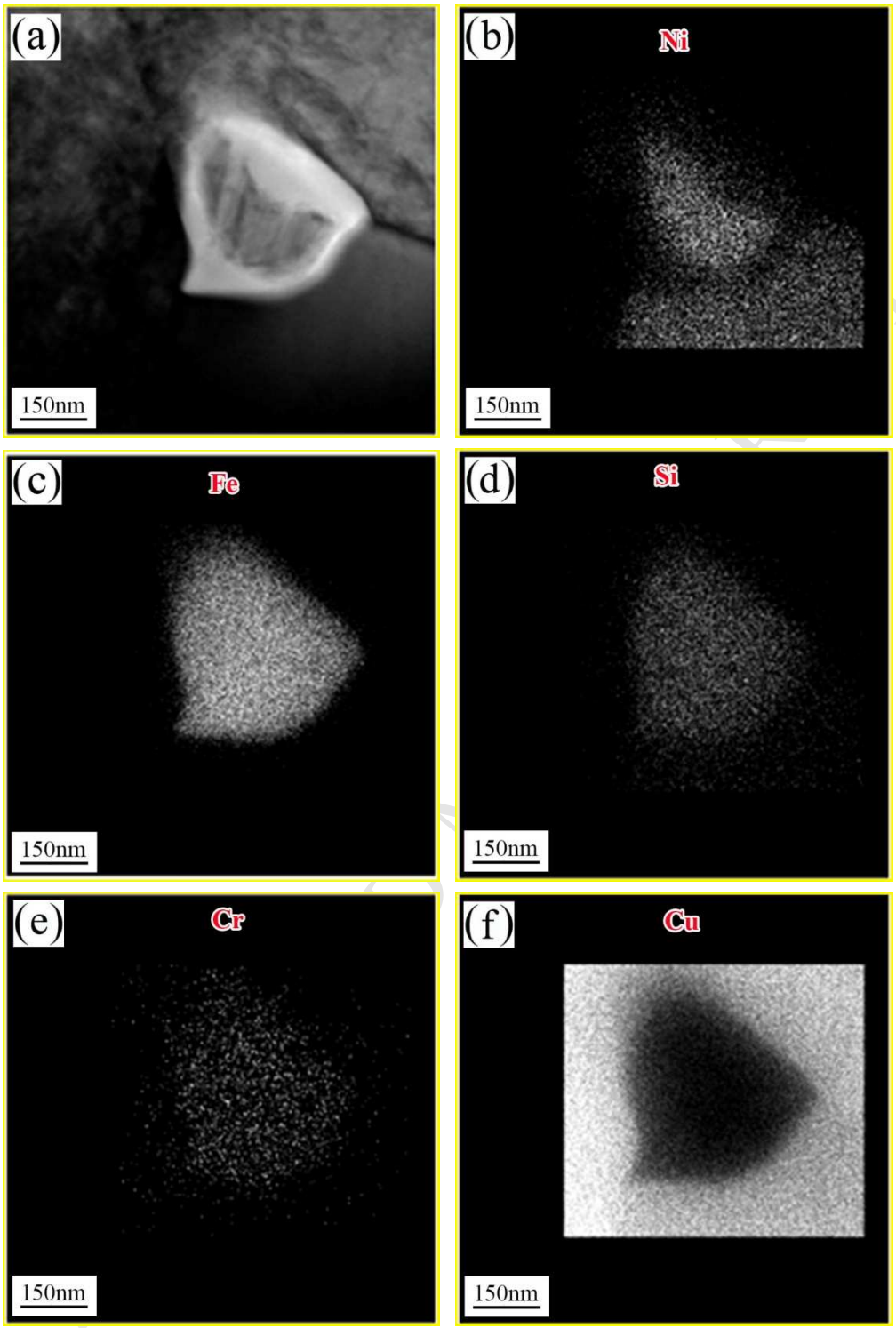

Fig. 5 (a) TEM image and (b)~(f) composition mapping of nano-scaled particles precipitated in the Cu-rich matrix in the upper layer.

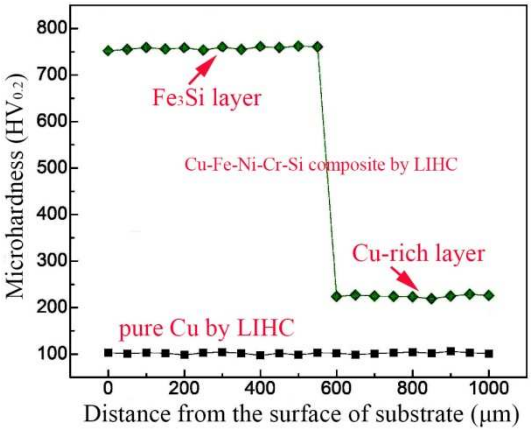

Fig. 6 Microhardness characteristic of the immiscible composite.

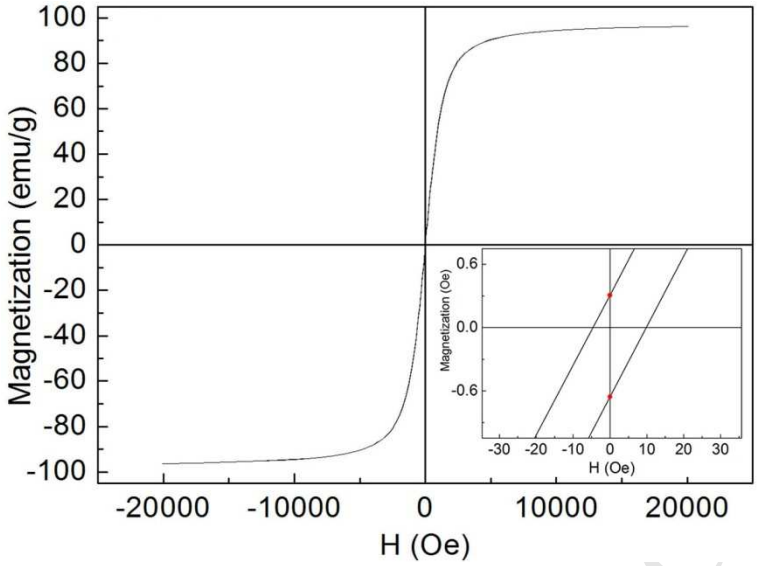

Fig. 7 Magnetic hysteresis loop of the immiscible composite at 300 K.

Highlights

1. Composite consists of Cu_p embedded in Fe_3Si matrix and Fe_p dispersed in ε-Cu matrix.

2. Immiscible composite exhibits a "bilayer microhardness".

3. Immiscible composite has high saturated magnetization (96.2 emu/g).

4. Immiscible composite exhibits a low coercivity (7.24 Oe).